



Controlled generation of periodic vortical gusts by the rotational oscillation of a circular cylinder and attached plate

Matthew Rockwood¹ · Albert Medina¹

Received: 21 August 2019 / Revised: 29 December 2019 / Accepted: 6 January 2020 / Published online: 12 February 2020
© Springer-Verlag GmbH Germany, part of Springer Nature 2020

Abstract

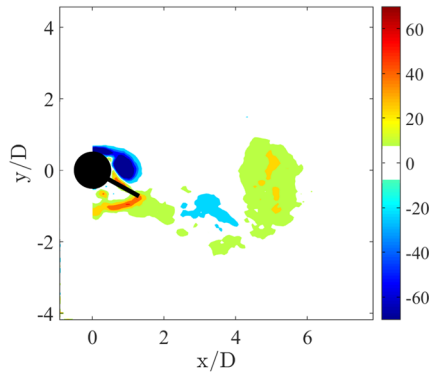
Understanding the interaction of vortical gusts and unsteady wing kinematics is crucial to the operation of small aircraft in urban or turbulent environments. Studies investigating this interaction require adequate control of a vortical gust generator to consistently produce the desired vortical gusts for study. Previous studies have focused on the pitching or heaving of airfoils to generate vortical gusts. The current study focuses on the characterization of the vortex shedding process for a rotationally oscillating circular cylinder with an attached one-diameter long plate. When this vortical gust generator is actuated in relatively small sinusoidal motions, von Kármán vortices can be generated in a controllable and repeatable fashion over a large range of oscillation frequencies that are significantly different than the natural shedding frequency of the static cylinder, and without the generation of any additional unwanted vorticity. Fine tuning of the actuation parameters allows for the control of the vortex strength, frequency, and transverse location.

✉ Matthew Rockwood
mrockwood@morsecorp.com

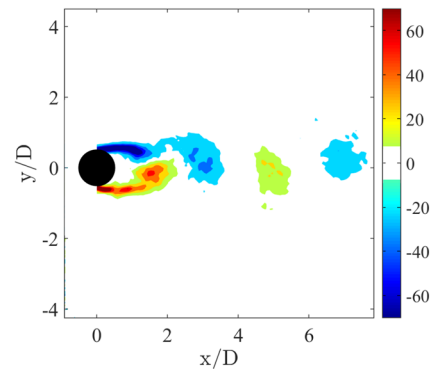
Albert Medina
alberto.medina.3@us.af.mil

¹ Aerospace Systems Directorate WPAFB, AS&M,
Aerodynamic Technology Branch, Aerospace Vehicles
Division, Dayton, OH 45433, USA

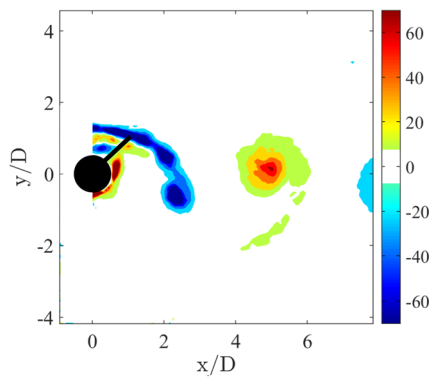
Graphic abstract



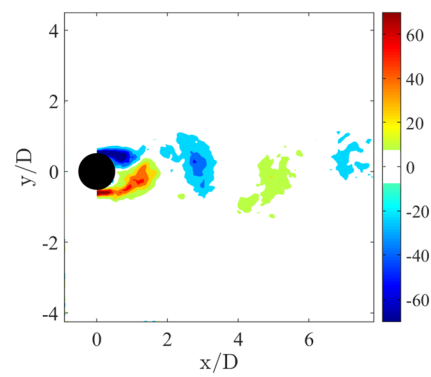
Cylinder-plate case 1



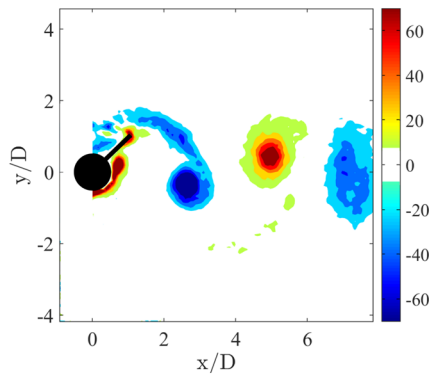
Static cylinder



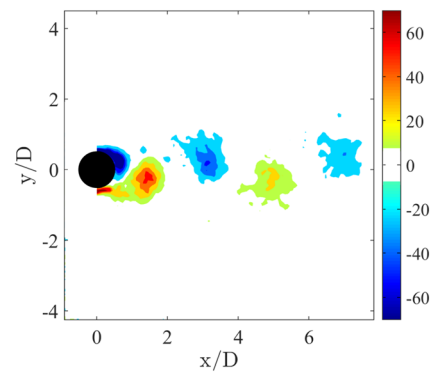
Cylinder-plate case 5



Cylinder case 6



Cylinder-plate case 9



Cylinder case 10

Vorticity contours for various rotational cases.

1 Introduction

Studies investigating the interaction between unsteady

aerodynamics and vortical gusts require adequate control of a vortical gust generator to allow for synchronization between the incoming vortices and the kinematics of the airfoil (Medina

et al. 2019). A simple example of a vortical gust generator is a circular cylinder immersed in a transverse flow. The resulting von Kármán vortex street can be thought of as a periodic series of vortical gusts, and is a well-documented phenomenon that persists over a large range of Reynolds numbers (Williamson 1996). One downside of this vortex-dominated wake, along with those of bluff bodies in general, is that the vortex shedding process can become disrupted by vortex dislocations (Williamson 1992). These vortex disruptions can lead to a loss of coherence in the wake for short durations, which is detrimental for studies relying on consistent vortical gusts. Additionally, the desire to synchronize the kinematics of a downstream airfoil to an oncoming vortex wake can benefit from the ability to control the vortex shedding frequency independent of the flow speed, as physical constraints often limit the range of freestream velocities that can be considered while maintaining a specific kinematic profile. This control is lacking for a static cylinder, where the vortex shedding frequency is fixed for a given set of flow conditions (Fey et al. 1998).

One strategy to improve the control of vortices shed from a circular cylinder is to rotationally oscillate the cylinder in a periodic sinusoidal fashion, as first studied by Okajima et al. (1975). The rotational oscillation of a circular cylinder about its axial coordinate has been studied at length numerically (Cheng et al. 2001; Lu and Sato 1996; Choi et al. 2002; Mittal et al. 2017; Aguedal et al. 2018) and experimentally (Tokumaru and Dimotakis 1991, 1993; Fujisawa et al. 1998; Thiria et al. 2006). These studies have determined that the vortex shedding in the wake of a rotationally oscillating circular cylinder can be drastically modified through large or fast enough rotations at a variety of frequencies over a range of Reynolds numbers from 150 to 3×10^4 . Different motions can generate multiple vortices of the same sign per period, or strengthen or weaken the naturally occurring von Kármán vortices (Tokumaru and Dimotakis 1991). Of particular interest to the current study is that multiple studies have determined lock-on frequencies for specific rotational parameters. The vortex wake is said to be locked on when vortices are shed from the rotationally oscillating cylinder at the same frequency as the oscillation in what amounts to a disruption of the natural shedding frequency for the given flow parameters. Different rotational oscillations of the cylinder can result in vortex shedding frequencies at significantly different frequencies than that of the static cylinder for the same flow conditions.

The most commonly reported parameter for the control of vortices with rotational oscillation is the normalized peak rotation rate, Ω (Tokumaru and Dimotakis 1991). The normalized peak rotation rate is defined as,

$$\Omega = v_{\theta, \max} / U_{\infty} = \omega D \theta_{\max} / 2U_{\infty}, \quad (1)$$

where $v_{\theta, \max}$ is the peak circumferential velocity, U_{∞} is the freestream velocity, ω is the rotation rate, D is the cylinder

diameter, and θ_{\max} is the maximum angular amplitude (Thiria et al. 2006). This parameter is the ratio between the maximum circumferential velocity of the cylinder and the freestream velocity. Generally, a certain threshold of Ω is needed to control the generation of vortices at a specific frequency. At an Ω value of eight, vortex lock-on can occur at frequencies at least ten times higher than the natural shedding frequency of a static cylinder (Tokumaru and Dimotakis 1991). While rotationally oscillating cylinders can provide vortex lock-on over a range of rotational frequencies, they are limited in their control of vortex strength and location due to the high rotational rates required to maintain vortex lock-on at frequencies significantly higher or lower than the natural shedding frequency (Thiria et al. 2006). A preferred vortical gust generation system could dictate the location, strength, and frequency of vortices based on the amplitude and frequency of the rotational oscillation.

A potential method for providing improved control over vortical gust generation was briefly studied by Myose and Heron (2009), where they attached a fixed plate normal to the cylinder surface, and then rotationally oscillated the entire cylinder-plate assembly in an attempt to generate consistent vortices interacting with a downstream pitching delta wing. The study had some difficulties with the experimental apparatus, and no characterization of the rotating cylinder-plate assembly was provided. This method of rotating the plate with the cylinder is in contrast to previous studies where splitter plates were placed upstream or downstream of cylinders, and were fixed or free to rotate [see e.g., Unal and Rockwell (1988); Xu et al. (1990); Cimbala and Garg (1991); Kwon and Choi (1996); Hwang et al. (2003); Lu et al. (2016)].

Previously studied methods for generating vortical gusts include pitching flat plates or airfoils (Biler et al. 2019) or a rapid change in heave direction of a flat plate (Hufstedler and McKeon 2019). Biler et al. (2019) utilized a flat plate pitched 180° about its midchord to generate a vortical gust. This method successfully generated a repeatable vortical gust, but the resulting wake also included nearby oppositely signed vorticity due to the motion of the plate [(see for example, Fig. 14 in Biler et al. (2019)]. The heaving motion of a flat plate studied by Hufstedler and McKeon (2019) was motivated by the desire to limit the test article's exposure to the wake of the gust generator. While successful, this technique yielded vortices with relatively low strength, and aggressive mechanical accelerations would be required to generate vortices with higher strengths. These methods of vortical gust generation were not pursued due to concerns about the formation of undesired vortical structures from pitching airfoils or flat plates, the experimental complexity of heaving systems compared to rotating systems, and the desire to generate strong, consistent, and periodic vortical gusts without the generation of any additional vorticity.

The current study also attempts to realize additional control authority over the vortex wake through the interaction between the attached plate and the shear layers on both sides of the cylinder.

The current study seeks to characterize the wake of a rotationally oscillating cylinder both with and without an attached plate, and compare them to the baseline static cylinder wake. The main metrics of comparison are the vortex strength found using circulation, the cycle-to-cycle consistency of the vortex location found using Γ_1 , and the range of lock-on frequencies for a fixed amplitude of rotational oscillation.

2 Experimental setup

Experiments were performed in the US Air Force Research Laboratory's Horizontal Free-surface Water Tunnel. The tunnel has a 4:1 contraction and a 46 cm wide by 61 cm high test section with a free surface, a speed range of 3–105 cm/s, and a freestream component of turbulence intensity of 1.0% at 5–40 cm/s. A transparent polycarbonate circular cylinder that was machined on a lathe with a 2.54 cm diameter and a 44.6 cm length was placed spanning the width of the tunnel between two 0.6 cm thick end plates. The end plates contained the support structure needed to maintain the cylinder position during oscillation, and were tapered to the wall near the cylinder location to minimize flow separation. The rotation axis was at the center of the circular cross-section of the cylinder. The cylinder was placed at roughly the centerline of the test section height. The cylinder-plate assembly used the same cylinder, but with a 2.54 cm long (1 diameter) clear acrylic plate that was 0.32 cm thick attached normal to the cylinder surface. The freestream speed was kept constant at 0.3 m/s, resulting in a Reynolds number based on cylinder diameter of 7600. The rotation of the system was driven by a gear and belt that were recessed into one of the end plates along the wall of the test section. The belt was driven by an Applied Motion HT23-598DC stepper motor and STR4 microstepper drive placed outside of the test section. A schematic of the experimental setup can be seen in Fig. 1.

The performance of the stepper motor and microstepper drive was evaluated to ensure the prescribed motion was followed. Angular position was measured via optical encoder with 2000 counts per revolution. The comparison between commanded position and encoder output for the cylinder driven with $\theta_0 = 45^\circ$ at $f = 2.617$ Hz reveals preservation of peak-to-peak amplitude and actuation frequency of the cylinder-plate test article, as shown in representative drive period in Fig. 2. A minor phase lag in encoder output from the commanded position of 0.065 radians does emerge, amounting to no more than 1.5° of error in instantaneous angular position, as shown in Fig. 2a. These deviations are predominantly

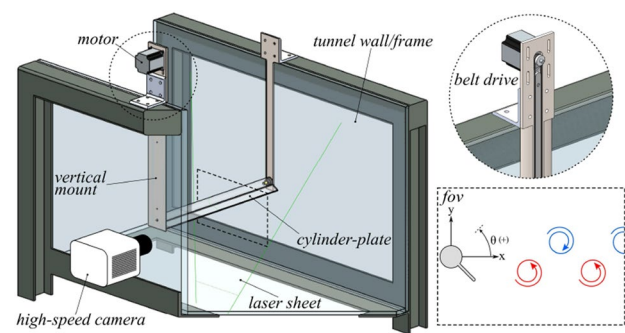


Fig. 1 Schematic of the rotating cylinder-plate assembly

sustained during peak angular velocity. However, it is noted that the minor lag is on par with the temporal resolution of the motor control software. Furthermore, experiments performed with the motor unloaded in air yielded the same results (Fig. 2b), thus ensuring motor operations in driving the cylinder-plate assembly were not torque limited in the most demanding case investigated in this study.

The frequencies, amplitudes, and corresponding normalized peak rotation rates studied are shown in Table 1. The same 12 cases were studied for both the rotating cylinder and the rotating cylinder-plate assembly. The frequencies and amplitudes were chosen to evaluate the ability of the vortex generator to achieve vortex lock-on over a wide range of frequencies and multiple amplitudes, constrained by the physical capabilities of the stepper motor driving the system. The amplitude, θ_{\max} , is measured from a reference line parallel to the streamwise flow on the downstream side of the cylinder. The Strouhal number (non-dimensional frequency) is defined as:

$$St = fD/U_\infty, \quad (2)$$

where f is the frequency. The Strouhal number associated with the natural shedding frequency, St_n , of the static cylinder at this Reynolds number was 0.202, and will be referred to as the natural Strouhal number. Strouhal numbers significantly higher than the natural Strouhal number were difficult to attain with the selected stepper motor due to the large torque required to overcome the forces imposed by the rotation of the cylinder-plate assembly, so the Strouhal number sweep focused on Strouhal numbers lower than the natural Strouhal number.

Time-resolved particle image velocimetry (PIV) measurements were planar, confined to the in-plane velocity field, and were taken at spanwise center of the cylinder. The tunnel was seeded with polyamide particles with a 20 μm diameter (LaVision, specific gravity = 1.03) and illuminated by an Nd:YLF laser sheet (Photonics Industries DM50-527, 55 mJ/pulse, 10 kHz max) oriented in the streamwise

Fig. 2 Encoder results

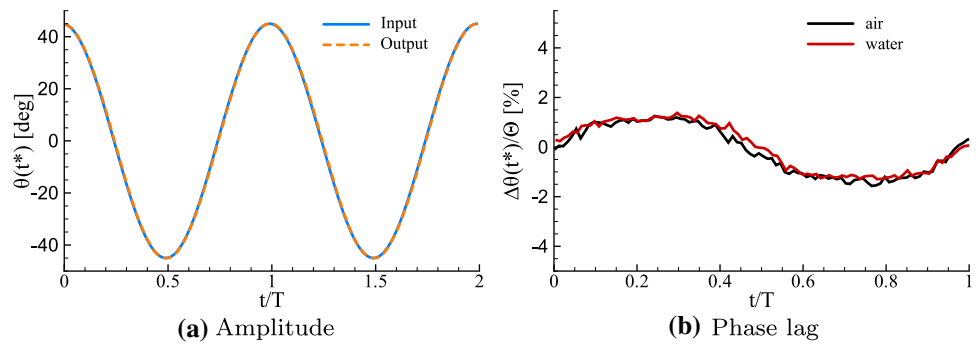


Table 1 Test parameters for the rotating cylinder and the cylinder-plate assembly

Case	St	Frequency ratio, St/St_n	Amplitude, θ_{max}	Ω
1	0.06	0.3	$\pi/4$	0.15
2	0.06	0.3	$\pi/6$	0.10
3	0.10	0.5	$\pi/4$	0.25
4	0.10	0.5	$\pi/6$	0.17
5	0.14	0.7	$\pi/4$	0.35
6	0.14	0.7	$\pi/6$	0.23
7	0.18	0.9	$\pi/4$	0.45
8	0.18	0.9	$\pi/6$	0.30
9	0.20	1.0	$\pi/4$	0.50
10	0.20	1.0	$\pi/6$	0.33
11	0.22	1.1	$\pi/4$	0.55
12	0.22	1.1	$\pi/6$	0.36

direction. Images were recorded by one high-speed camera (PCO Dimax S4, 4 MP, 1279 fps at max resolution) that was located at $x/D = 3.5$, $y/D = 0$. Velocity vectors were calculated using Fluere version 1.3. Two passes of interrogation areas, with initial and final sizes of 64 px^2 , and 32 px^2 , respectively, were used to determine the particle displacements from double frame images sampled at a rate around 400 Hz during continuous operation. An interrogation area overlap of 50% was used. The resultant vector fields contained 123×123 vectors with a spatial resolution of $(x/D, y/D) = (0.072, 0.072)$. No interpolation was performed on the calculated vector fields prior to post-processing. Upstream portions of the flowfield ($x/D < 0$) were partially blocked either by shadows or the cylinder support structure, and therefore the results in this region were masked.

Error estimates in the calculation of PIV vectors were conducted using the methods and figures in chapter 5.5 of Raffel et al. (2018). For portions of the flow field with low gradients, the particle displacement error is roughly 0.05 pixels, corresponding to a 0.5% error. In regions with large velocity gradients, the particle displacements are locally

much higher, as Fluere does not support deforming interrogation areas. The errors in this region can reach up to 1.05 pixels, corresponding to an error up to 8.8%. These errors are very localized, and the values reported here are worst case estimates based on known parameters and the simulation results present in Raffel et al. (2018). Throughout the flow field, the vast majority of errors are 1% or less.

The PIV results presented below were primarily phase-averaged over multiple periods of cylinder shedding using the average Strouhal number. 3500 images were used for each test case, and the number of periods of data collected varied with the Strouhal number of oscillation from six periods for the lowest Strouhal number up to 23 periods for the highest. Cases 1, 3, 5, and 6 for the rotating cylinder were phase-averaged using proper orthogonal decomposition (POD) instead of utilizing the average Strouhal number due to prohibitively low consistency in vortex shedding. The phase-averaging techniques used are discussed in more detail in the following section.

3 Methodology

Velocity vector fields generated by PIV were analyzed to determine the average strength and consistency of the vortices shed over multiple cycles. The strength of the vortices was determined using circulation, where a phase-averaged vortex with its center located five diameters downstream of the cylinder center was bounded by a rectangular area from four to six diameters downstream, and 2.5 diameters above and below the wake centerline. All of the positive vorticity within this area was included in the circulation calculation. Circulation is defined, utilizing Stoke’s theorem, as:

$$-\Gamma = \oint_{\partial A} \mathbf{u} \cdot d\mathbf{s} = \iint_A \boldsymbol{\omega} \cdot d\mathbf{A}, \tag{3}$$

where ∂A is the boundary of area A , \mathbf{u} is the velocity field, $\boldsymbol{\omega}$ is the vorticity, $d\mathbf{s}$ is aligned tangent to an infinitesimal portion of the boundary, and $d\mathbf{A}$ is the normal vector to an infinitesimal portion of the area. While the integration area

chosen can have a significant effect on the resulting circulation values for a given vortex, von Kármán vortices are distinct enough at the wake location used for this study that variations in the chosen area had no noticeable effect on the circulation results as long as the area chosen was large enough to encompass the entire vortex. The same area of consideration was used for each case.

The cycle-to-cycle consistency of the vortex center location is a measure of how successful the chosen oscillations were at driving consistent vortex shedding. The vortex center location was determined using the Γ_1 criterion developed by Graftieux et al. (2001). The value of Γ_1 at a point, P , is defined as:

$$\Gamma_1(P) = \frac{1}{S} \int_{M \in S} \frac{(PM \wedge U_M) \cdot z}{\|PM\| \cdot \|U_M\|} dS \tag{4}$$

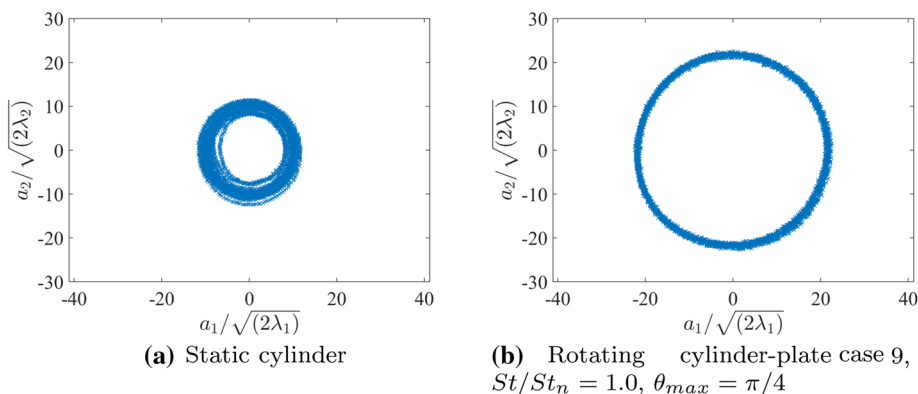
where S is a two-dimensional area surrounding P , M is a point within S , and z is the unit normal to the data plane. PM is the radius vector from point P to point M , and U_M is the velocity vector at point M . This method determines the center of rotation of a vortex by summing the local flow angles of points within a user-defined area. The center of rotation is located at the maximum value of Γ_1 . The main parameter the user controls is the size and shape of the area of consideration around each point. To remove subjectivity from this portion of the study, a parameter sweep was conducted where a square area was varied from $0.5D$ a side to $2.0D$ per side, and the resulting vortex center locations were compared. A similar vortex center location (within ± 1 velocity grid point) was found for side lengths between $1.2D$ and $1.8D$, with increasing variation in the result as the side length was increased or decreased from that range. A value of $1.6D$ was chosen, as it was roughly in the center of the range of side lengths with consistent vortex center locations. The same velocity fields were used in the Γ_1 calculations as in the circulation calculations, with positive vortices located with their centers at approximately $x/D = 5$.

The snapshot proper orthogonal decomposition (POD) technique developed by Sirovich (1987) was used to decompose the velocity fields collected by PIV into spatial eigenmodes and temporal coefficients on an energy basis. In periodic vortex-dominated flows, POD modes are found to occur in pairs that represent the orthogonal components of the harmonics of the vortex shedding process (Oudheusden et al. 2005). In the current study, the first two modes combined contained 34% of the total energy of the flow for the static cylinder case and are associated with the convection of the von Kármán vortices. The energy contained in the first two modes combined increased up to a maximum of 74% for the rotating cylinder-plate case 9.

Figure 3 shows the temporal coefficients of the first two modes (a_1 and a_2) normalized by their energy, where each data point is the location of normalized a_2 versus a_1 for a velocity field snapshot. The variation in the radius of the circle is thought to be caused by variations in the periodicity of the von Kármán vortex shedding (Perrin et al. 2007). Case 9 for the rotating cylinder-plate had less variation in the periodicity of vortex shedding compared to the static case, and this can be visualized in Fig. 3 by a larger amount of variation in the radius of the circle for the static case compared to the rotating cylinder-plate case 9.

Each period of vortex shedding was determined by the number of files it took to make a complete revolution around the circle generated by the first two temporal POD coefficients. The result was then averaged over the total number of cycles of vortex shedding that were recorded to determine the average vortex shedding frequency. This value was used as the frequency at which to phase-average the velocity fields for most cases. This was done by dividing one period of motion into 36 equally sized bins in time. Every velocity field that fell within the same bin was phase-averaged together. 36 bins were sufficient to provide time-resolved analysis of the flow physics, as well as converged, phase-averaged velocity fields. This method of phase-averaging will be referred to as the average frequency method.

Fig. 3 Normalized second versus first temporal coefficients found using POD



For cases 1, 3, 5, and 6 for the rotating cylinder, the rotational motion of the cylinder was not significant enough to drastically change the flow field from that of a static cylinder, so the vortex shedding process suffered from vortex dislocations during data collection, and therefore the average frequency method for phase-averaging was not utilized. For these cases, bins of 10° width in the respective a_2 versus a_1 plots were used to determine which velocity fields had similar spatial structure. All velocity fields that were within the same bin were then phase-averaged. This resulted in 36 phase-averaged velocity fields, the same number used for the average frequency method. Vorticity contours, circulation values, and vortex center results between the average frequency and POD methods of phase-averaging for the remaining cases were compared, and negligible differences were found.

4 Results

Phase-averaged vorticity contours for the wakes generated by several representative rotating cylinder cases, as well as the static case are shown in Fig. 4. The results for the static cylinder shown in Fig. 4b are representative of a von Kármán vortex street, with periodic vortices shedding from shear layers above and below the cylinder. In comparison, rotating case 1 in Fig. 4a is at a Strouhal number that is only 30% of the natural Strouhal number of the static cylinder. Due to the low amplitude and frequency of oscillation, vortex lock-on does not occur, as the vortices are shed at the same frequency as in the static case. The inability of the cylinder motion to achieve vortex lock-on is also present for rotating cases 5 and 6 (Fig. 4c, d). In fact, the rotation process may interfere with the natural shedding process, leading to an apparent decrease in coherency in the phase-averaged vorticity fields compared to that of the static cylinder. There is no evidence of a coherent vortex core in the vorticity contours for rotating cases 5 and 6 in the positively signed vortex at $x/D = 5$ compared with the static case. At rotation rates at the natural Strouhal number (Fig. 4e, f), the vortex wake is comparable to that of the static case. The main difference is that the von Kármán vortices form significantly closer to the cylinder. This could allow airfoils to be placed closer to the downstream extent of the cylinder without interfering with the vortex formation process.

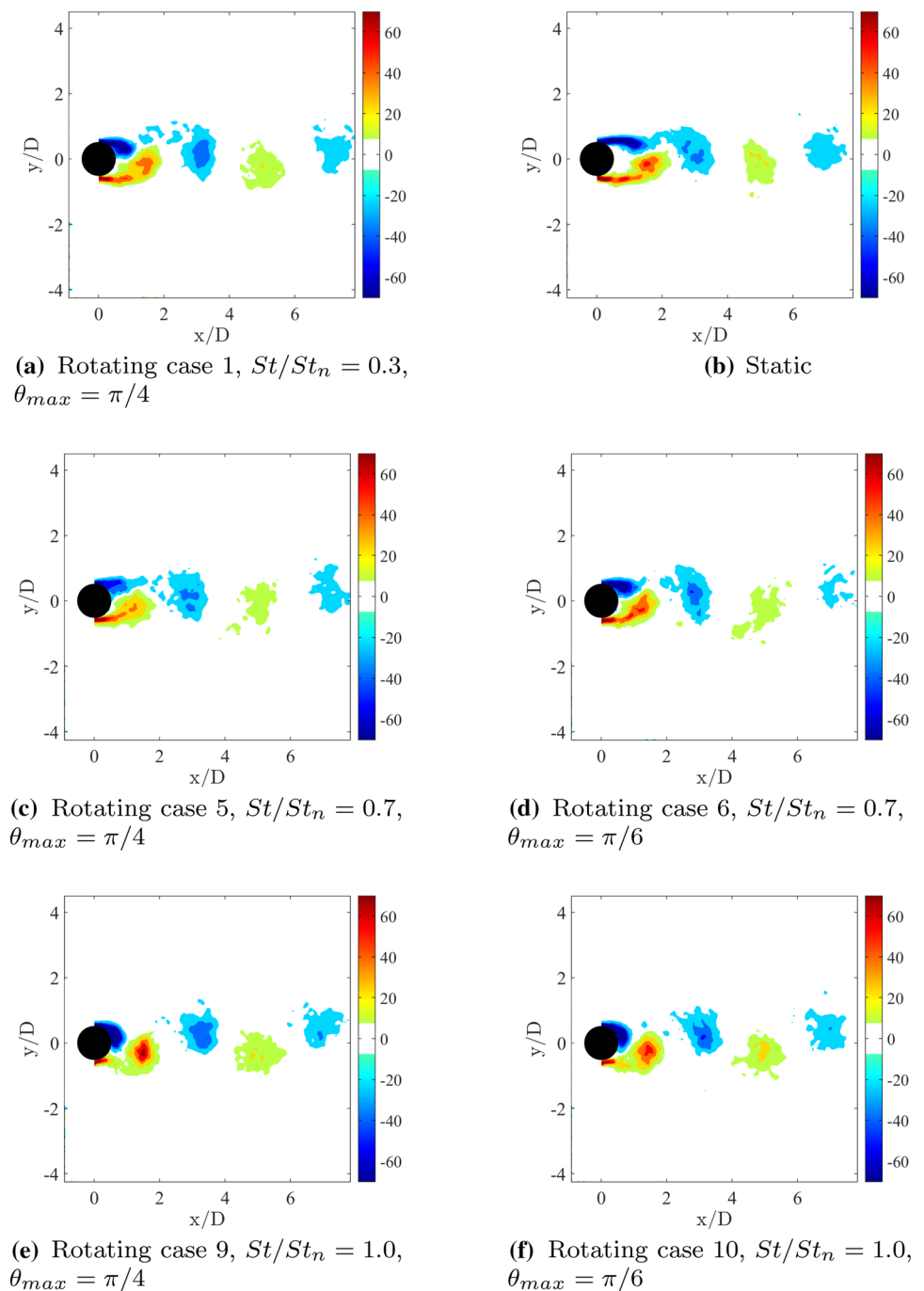
Figure 5 shows phase-averaged vorticity contours for selected rotating cylinder-plate cases. The vorticity fields highlight significant changes to the vortex wake structure due to the motion of the cylinder-plate assembly compared to the rotating cylinder cases displayed in Fig. 4. In cases 1 and 2 at frequencies that are 30% of the natural Strouhal number, the vortex wake appears to be locked on for both angular amplitudes in the Fig. 5a and b. Although locked on

vortex shedding was one goal of the study, the other was to have one distinct vortex of each sign shed from the cylinder-plate assembly for each oscillation period, similar to the von Kármán vortex street for a static cylinder. In Fig. 5a and b, there is additional negatively signed vorticity accompanying the positively signed vortex downstream. The low oscillation Strouhal number resulted in vorticity of the opposite sign being generated by the interaction of the shear layer and plate before being shed with the vortex. This process is highlighted in more detail in Fig. 6. The positively signed vortex at $x/D = 5$ is also significantly larger and more diffuse than those present in the static and rotating cylinder cases. The vortices in this case form in the separated flow region just downstream of the plate (Fig. 6a–c), similar to the formation process for a static cylinder. The main difference in the formation process with the plate is that the shear layer on the side of the cylinder-plate is deflected towards shifts almost half a diameter away from the surface of the cylinder (Fig. 6a). The vorticity in the shear layer has the opposite sign of the forming von Kármán vortex, and a portion of the shear layer is shed with the main vortex when the plate begins moving towards the wake centerline from its maximum location (Fig. 6d–f).

For cases 5 and 6 at oscillation frequencies that are 70% of the natural Strouhal number (Fig. 5c, d), a wake very reminiscent of the natural von Kármán wake is captured, but locked on to the oscillation Strouhal number. Clear vortices with no oppositely signed vorticity are present, but the vortices do have a slight tail for both angular amplitudes. The formation process for these vortices is different than that discussed for the rotating cylinder-plate cases 1 and 2. For Ω values above about 0.3, the shedding process changes so the vorticity that makes up the bulk of the von Kármán vortices is entrained into a forming vortex near the tip of the plate during its motion instead of in the wake region behind the cylinder. At this Strouhal number, case 5 is above this Ω value, and case 6 is below it. Therefore, case 6 is still generating the majority of its vorticity due to the momentum deficit behind the cylinder and plate. Case 5, on the other hand, is generating vorticity more in line with the method that vortices are generated by wings pitching about their leading edge.

For cases 9 and 10, shown in Fig. 5e and f, the cylinder-plate assembly is driven at the natural Strouhal number. This results in a von Kármán wake with significantly higher vorticity values in the vortex cores, as well as more coherent vortices compared to the static case. Both Ω values are now above 0.3, so both angular amplitudes are entraining the bulk of their vorticity from the tip of the plate. One major departure from the flow field seen for the static cylinder wake in Fig. 4b is the transverse (y/D) location of the vortices. For the static cylinder, the negatively signed vortices were at larger y/D values than the positively signed vortices,

Fig. 4 Vorticity contours for representative static and rotating cylinder cases

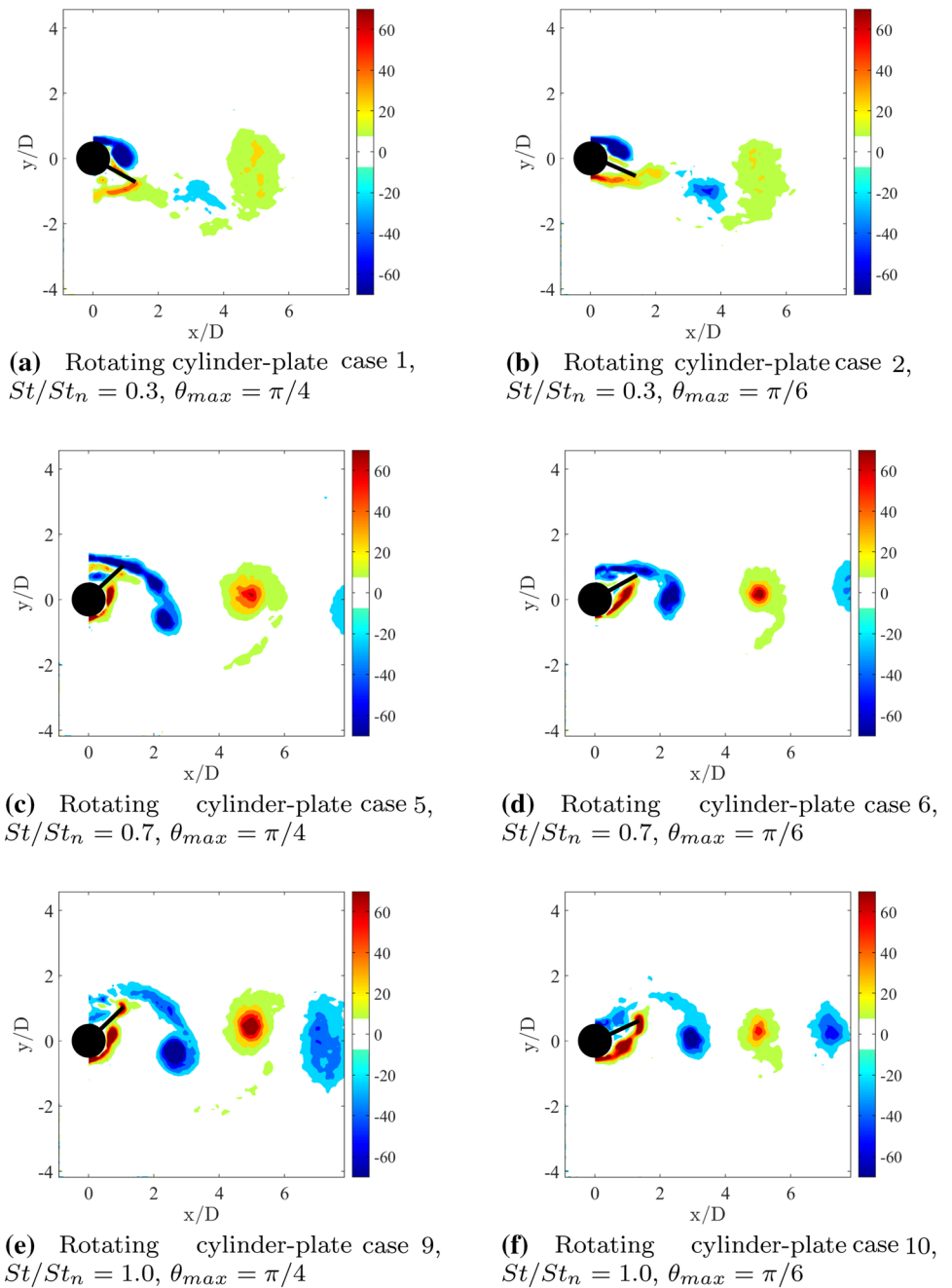


corresponding to their respective shear layer sides. For the rotating cylinder-plate case 9, the vertical location of these vortices has switched, and the positively signed vortices are at larger y/D values than the negatively signed vortices. This is indicative of a reverse von Kármán wake, which is associated with thrust production. Reducing the amplitude of the oscillation (Fig. 5f) results in vortices with vertical locations roughly constant at the cylinder centerline. By further refinement of the oscillation amplitude, control of the vertical

locations of the resulting vortices should be realizable, up to a certain distance from the wake centerline.

Additional details of the lock-on Strouhal numbers, cycle-to-cycle consistency of vortex locations, and vortex strengths can yield insights into the ability of the rotating cylinder and the rotating cylinder-plate assembly to generate controlled vortical gusts. Figure 7 displays plots of the average shedding Strouhal number compared with the oscillation Strouhal number. Error bars of one standard deviation of the shedding Strouhal number are included. The solid black

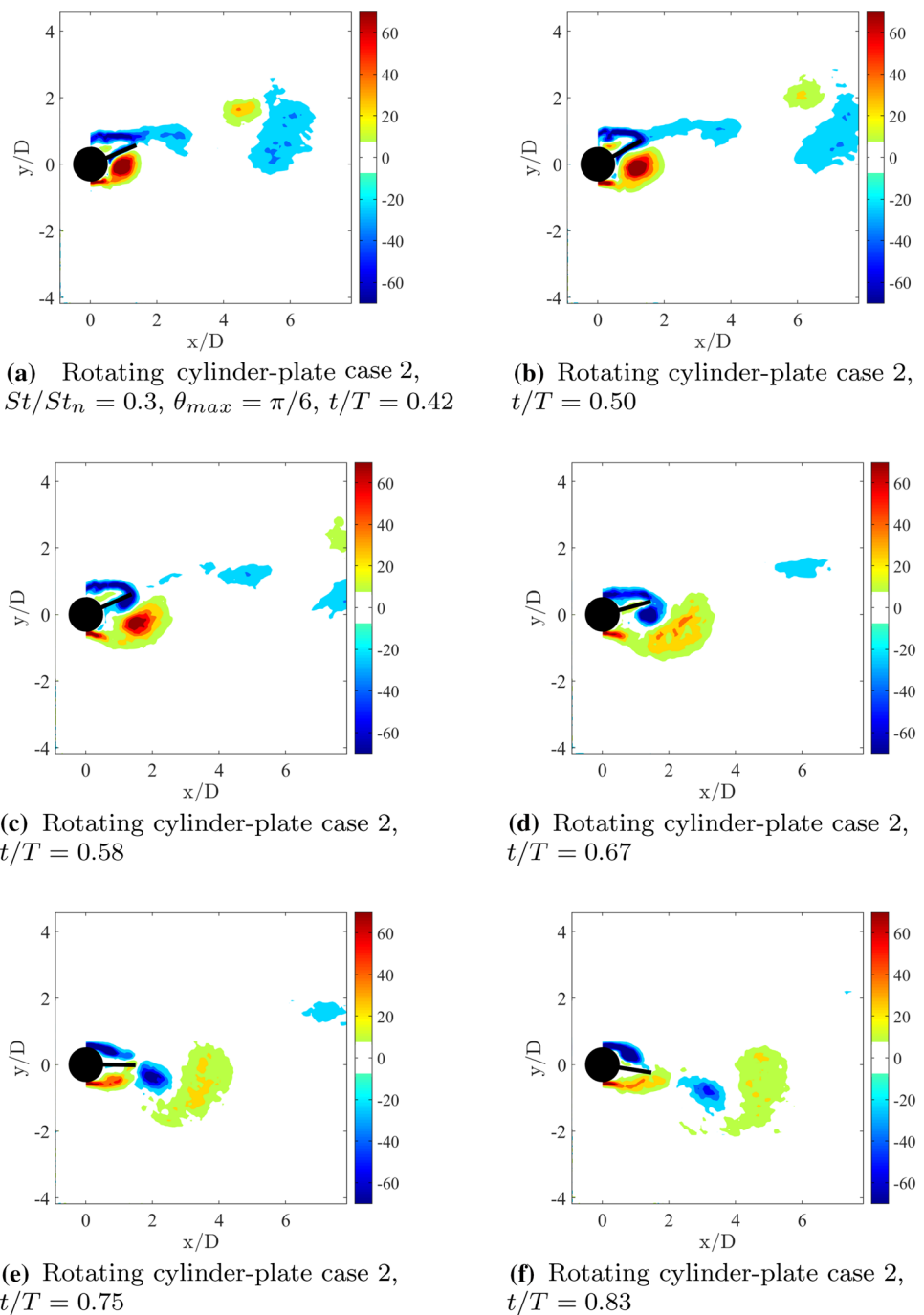
Fig. 5 Vorticity contours for representative rotating cylinder-plate cases



line is at equivalent oscillation and vortex shedding Strouhal numbers, and data points on that line signify cases that were locked on. The static cylinder natural Strouhal number and one standard deviation errors bars are shown in dashed and dash-dotted lines, respectively. The vertical dashed line is also at the natural Strouhal number for reference. For the $\pi/6$ angular amplitude cases shown in Fig. 7a, the rotating cylinder cases (blue diamonds) do not achieve vortex lock-on at Strouhal numbers at or below 70% of the natural Strouhal number. These cases maintain roughly the same Strouhal number as the natural Strouhal number of the static cylinder.

For oscillation Strouhal numbers within 10% above or below the natural Strouhal number, vortex lock-on did occur for the rotating cylinder, although the error bar for case 12 is large enough that it is not certain that lock-on did occur. The same range of lock-on Strouhal numbers is present in Fig. 7b for an angular amplitude of $\pi/4$, indicating that an even higher amplitude of motion would be required to achieve lock-on at oscillation Strouhal numbers further from the natural Strouhal number for the rotating cylinder. Errors bars for the rotating cylinder cases with vortex lock-on (cases 7 and 9) are comparable to or smaller than the error bars for the

Fig. 6 Vorticity contours highlighting the vortex formation and shedding process for rotating cylinder-plate case 2



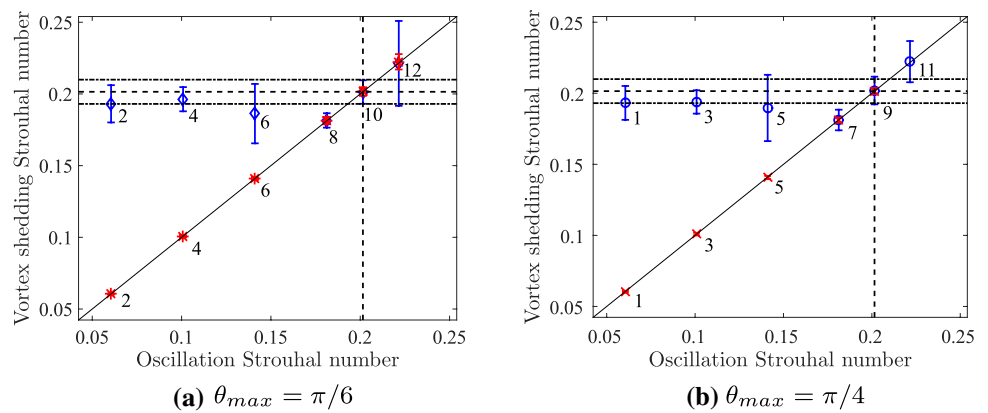
static cylinder, indicating that there may be an increase in the shedding frequency consistency for the von Kármán street by oscillating the cylinder wake at the natural Strouhal number at low amplitudes.

Vortex lock-on occurred for both of the amplitudes of cylinder-plate assembly oscillations (red asterisks and xs) across the entire range of Strouhal numbers tested. In fact, there is little to no cycle-to-cycle variation for any of the values below the natural Strouhal number as indicated by the near-zero error bars. The error bars for case 12 are still fairly

low, but are significantly higher than those of the other rotating cylinder-plate cases. This could be indicative of the stepper motor reaching the limit of its torque capabilities to drive accurate motion of the cylinder-plate assembly. Overall, the rotating cylinder-plate assembly was very successfully in maintaining a consistent frequency of vortex shedding for the angular amplitudes studied.

The location of the vortex center of each instantaneous velocity field that occurred within the same shedding phase over multiple cycles of vortex shedding was

Fig. 7 Vortex shedding Strouhal number versus oscillation Strouhal number for the static cylinder (dashed black lines with solid black error bars), rotating cylinder ($\theta_{max} = \pi/6$ in blue diamonds and $\theta_{max} = \pi/4$ in blue circles), and rotating cylinder-plate ($\theta_{max} = \pi/6$ in red asterisks and $\theta_{max} = \pi/4$ in red xs). Individual data points are labeled by their case numbers

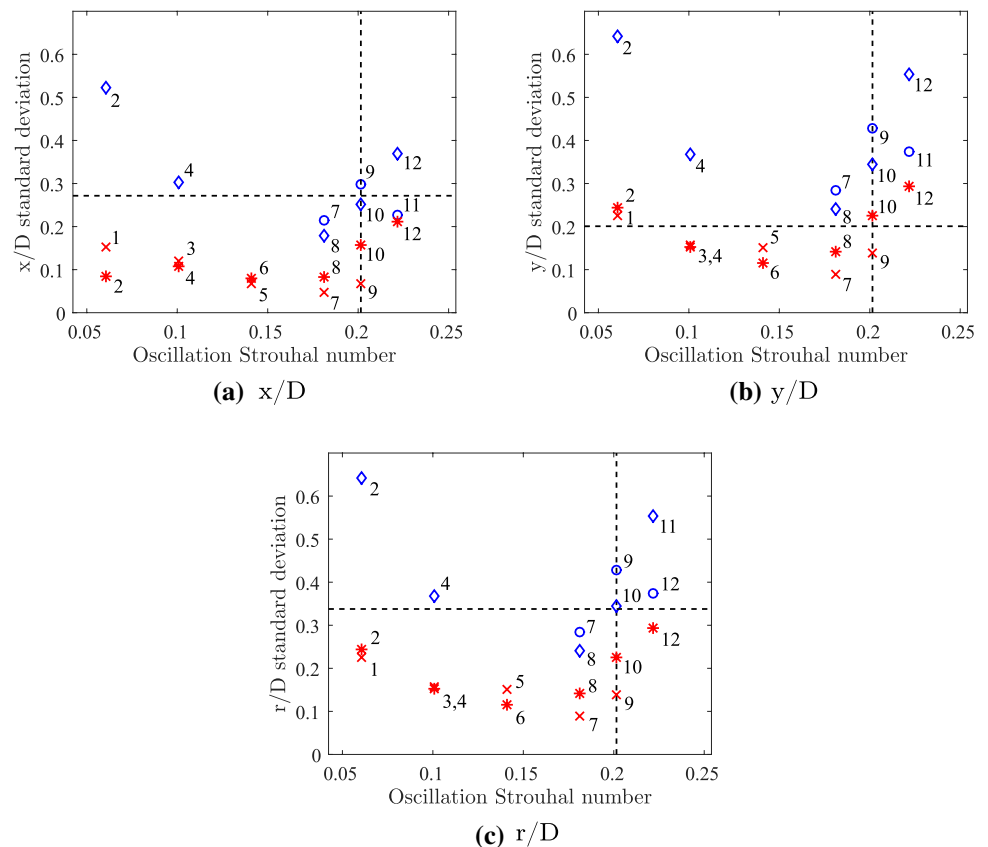


determined using Γ_1 . The standard deviation in x/D , y/D , and r/D (radial distance) from the average vortex center location was calculated as a metric for the consistency of vortex center locations from cycle to cycle. A low standard deviation means the vortices were consistently near the same location from period to period, and a higher standard deviation means the vortices were less consistently located. The standard deviation in x/D shown in Fig. 8a yields information in line with the error bars presented in Fig. 7a and b. The vortex x/D location is directly tied to the frequency of vortex shedding, so inconsistencies in the shedding Strouhal number directly translate to

inconsistencies in the streamwise vortex location from period to period. Cases with vortex lock-on and small error bars in Fig. 7 had lower x/D standard deviations than the static case shown with the horizontal dashed black line, and cases with large error bars in Fig. 7 had higher variation in streamwise vortex location.

Figure 8b shows the same results, but in the y/D , or transverse direction. The static case has a relatively low 0.2 y/D standard deviation as the vortices are fairly consistent in their transverse location due to the overall structure of the flow field generated by shear layers separating from the fixed geometry of the static cylinder. Most of the rotating

Fig. 8 Cycle-to-cycle standard deviation of vortex center locations for the static cylinder (dashed black lines), rotating cylinder ($\theta_{max} = \pi/6$ in blue diamonds and $\theta_{max} = \pi/4$ in blue circles), and rotating cylinder-plate ($\theta_{max} = \pi/6$ in red asterisks and $\theta_{max} = \pi/4$ in red xs). Individual data points are labeled by their case numbers



cylinder-plate assembly cases (red asterisks and xs) yielded lower y/D standard deviations for the shed vortices, with values less than half of that of the static case for an oscillation Strouhal number of 0.18. All of the rotating cylinder cases (blue diamonds and circles), and the highest and lowest Strouhal numbers for the rotating cylinder-plate assembly yielded less consistent vortex y/D locations. This could be due to the interaction between the cylinder motion and the shear layers resulting in the shear layers no longer remaining quasi-fixed in the same location relative to the cylinder, as in the static case.

The radial standard deviation is shown in Fig. 8c. The rotating cylinder-plate assembly had lower standard deviations than the static cylinder, with the best performance at cases equal to or below the natural Strouhal number. The only rotating cylinder cases that performed better than the static case were cases 7 and 8, just below the natural Strouhal number. This is in line with the findings of Fujisawa et al. (1998), where frequencies just below the natural Strouhal number were more receptive to relatively slow rotations of the cylinder than values above the natural Strouhal number.

The relative strength of the vortices was quantified using circulation values calculated from phase-averaged velocity fields, and the results are shown in Fig. 9. Only cases 11 and 12 for the rotating cylinder (blue diamonds and circles) generated vortices weaker than the static cylinder. Cases 1–6 for the rotating cylinder generated vortex strengths that were approximately the same as the static case. Cases 7 through 10 generated vortices slightly stronger than the static case, with the rotational Strouhal number at 90% of the natural Strouhal number yielding the strongest vortices. This is in

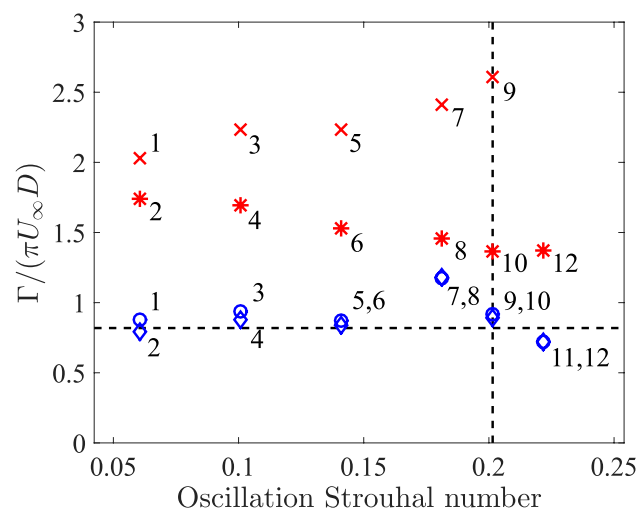


Fig. 9 Circulation values for the static cylinder (dashed black lines), rotating cylinder ($\theta_{max} = \pi/6$ in blue diamonds and $\theta_{max} = \pi/4$ in blue circles), and rotating cylinder-plate ($\theta_{max} = \pi/6$ in red asterisks and $\theta_{max} = \pi/4$ in red xs). Individual data points are labeled by their case numbers

line with the velocity fluctuation measurements of Fujisawa et al. (1998).

The cylinder-plate assembly generated two apparent tracks of vortex strengths. The $\pi/6$ angular amplitudes (red asterisks) created a lower branch of circulation values that were significantly higher than the static cylinder, but at a slightly decreasing strength with increasing Strouhal number. For cases with oscillation Strouhal numbers below 0.20, Ω is lower than 0.3, and the vortices formed in the recirculating wake region just behind the cylinder-plate. The vorticity entrained into vortices forming in this manner is primarily from the cylinder shear layer, with little to no contribution from the plate. This is a similar vortex formation process as that of a static or rotating cylinder. As the oscillation Strouhal number increases for those cases, the duration the plate spends at its maximum angle decreases, leaving less time for a vortex to form and to continue entraining vorticity from the shear layer, effectively reducing the strength of the vortex. Once $\Omega \geq 0.3$, the circulation levels off as the forming vortex also gains vorticity from the sweeping tip of the plate.

Cases with a $\pi/4$ angular amplitude for the rotating cylinder-plate yielded significantly higher vortex strengths than the static case. Cases 1, 3, and 5 are at or below $\Omega = 0.3$, and all have roughly the same circulation values. Cases 7 and 9 have Ω values of 0.45 and 0.50, respectively, and display a significant increase in circulation values with increasing Strouhal number. This is indicative of increased circulation being added to the von Kármán vortices by the increasing difference in velocity between the plate tip speed and the local velocity field as the Strouhal number increases. Specifically chosen oscillation amplitudes for the rotating cylinder-plate assembly can modify the strength of the generated vortical gusts independent of the oscillation Strouhal number. Therefore, this experimental vortical gust generation system provides the desired control of vortical gusts for interaction with downstream airfoils.

5 Summary

An experimental method utilizing a rotationally oscillating cylinder-plate assembly for generating consistent and controllable vortical gusts was tested for a range of forcing Strouhal numbers at two different angular amplitudes. The cylinder-plate assembly was comprised of a one-diameter long flat plate fixed normal to the cylinder. The entire cylinder-plate assembly was rotationally oscillated to generate vortical gusts. The results for the rotating cylinder-plate were compared with results at the same Reynolds number for a static cylinder and a rotating cylinder undergoing the same prescribed rotational oscillations. The rotating cylinder-plate assembly was able to achieve vortex lock-on over the entire range of frequencies tested, from 30 to 110% of the natural

Strouhal number. The rotating cylinder-plate also generated vortices with consistent locations from cycle to cycle. The rotating cylinder undergoing the same motion was only able to obtain vortex lock-on between 90 and 110% of the natural Strouhal number, and yielded less consistent vortex locations than the cylinder-plate cases.

At the angular amplitudes of $\pi/4$ and $\pi/6$ tested in this study, the circulation values of the von Kármán vortices shed by the cylinder-plate system were significantly higher than that of the static or rotating cylinders, and changing the amplitude of oscillation resulted in control of the vortex strength and transverse location. The rotational oscillation of a cylinder-plate assembly therefore allows for the control of the frequency and strength of consistent vortical gusts based on the actuation Strouhal number and oscillation amplitude chosen. This experimental method also results in significantly more consistent vortical gusts compared to the static cylinder wake, which allows for the synchronization of the vortical gusts with downstream wing kinematics.

References

- Aguedal L, Semmar D, Berrouk AS, Azzi A, Oualli H (2018) 3d vortex structure investigation using large eddy simulation of flow around a rotary oscillating circular cylinder. *Eur J Mech B Fluids* 71:113–125
- Biler H, Jones AR, Saritas M, Fenercioglu I, Cetiner Yildirim NL, Bronz M (2019) Investigation of force transients during transverse and vortex gust encounters. In: *AIAA Scitech 2019 Forum*, p 0636
- Cheng M, Liu G, Lam K (2001) Numerical simulation of flow past a rotationally oscillating cylinder. *Comput Fluids* 30(3):365–392
- Choi S, Choi H, Kang S (2002) Characteristics of flow over a rotationally oscillating cylinder at low Reynolds number. *Phys Fluids* 14(8):2767–2777
- Cimbala JM, Garg S (1991) Flow in the wake of a freely rotatable cylinder with splitter plate. *AIAA J* 29(6):1001–1003
- Fey U, König M, Eckelmann H (1998) A new Strouhal-Reynolds-number relationship for the circular cylinder in the range $47 < Re < 2 \times 10^5$. *Phys Fluids* 10(7):1547–1549
- Fujisawa N, Ikemoto K, Nagaya K (1998) Vortex shedding resonance from a rotationally oscillating cylinder. *J Fluids Struct* 12(8):1041–1053
- Graftieaux L, Michard M, Grosjean N (2001) Combining PIV, POD and vortex identification algorithms for the study of unsteady turbulent swirling flows. *Meas Sci Technol* 12(9):1422
- Hufstedler EA, McKeon BJ (2019) Vortical gusts: experimental generation and interaction with wing. *AIAA J* 57(3):921–931
- Hwang JY, Yang KS, Sun SH (2003) Reduction of flow-induced forces on a circular cylinder using a detached splitter plate. *Phys Fluids* 15(8):2433–2436
- Kwon K, Choi H (1996) Control of laminar vortex shedding behind a circular cylinder using splitter plates. *Phys Fluids* 8(2):479–486
- Lu L, Xi Guo, Gq Tang, Mm Liu, Cq Chen, Xie Zh (2016) Numerical investigation of flow-induced rotary oscillation of circular cylinder with rigid splitter plate. *Phys Fluids* 28(9):093.604
- Lu XY, Sato J (1996) A numerical study of flow past a rotationally oscillating circular cylinder. *J Fluids Struct* 10(8):829–849
- Medina A, Babu AV, Rockwood M, Gopalathnam A, Ahmed A (2019) Theoretical and experimental study of wake encounters on unsteady airfoils. In: *AIAA Scitech 2019 Forum*, p 0898
- Mittal H, Al-Mdallal QM, Ray RK (2017) Locked-on vortex shedding modes from a rotationally oscillating circular cylinder. *Ocean Eng* 146:324–338
- Myose R, Heron I (2009) Impingement of a von Kármán vortex street on a dynamically pitching delta wing part 2: Small cylinder results. In: *47th AIAA Aerospace Sciences Meeting including The New Horizons Forum and Aerospace Exposition*, p 96
- Okajima A, Takata H, Asanuma T (1975) Viscous flow around a rotationally oscillating circular cylinder. *NASA STI/Recon Technical Report N 76*
- Oudheusden BWv, Scarano F, Hinsberg NPv, Watt DW (2005) Phase-resolved characterization of vortex shedding in the near wake of a square-section cylinder at incidence. *Exp Fluids* 39(1):86–98
- Perrin R, Braza M, Cid E, Cazin S, Barthet A, Sevrain A, Mockett C, Thiele F (2007) Obtaining phase averaged turbulence properties in the near wake of a circular cylinder at high Reynolds number using POD. *Exp Fluids* 43(2–3):341–355
- Raffel M, Willert CE, Scarano F, Kähler CJ, Wereley ST, Kompenhans J (2018) *Particle image velocimetry: a practical guide*. Springer, Berlin
- Sirovich L (1987) Turbulence and the dynamics of coherent structures. I. Coherent structures. *Q Appl Math* 45(3):561–571
- Thiria B, Goujon-Durand S, Wesfreid J (2006) The wake of a cylinder performing rotary oscillations. *J Fluid Mech* 560:123–147
- Tokumaru P, Dimotakis P (1991) Rotary oscillation control of a cylinder wake. *J Fluid Mech* 224:77–90
- Tokumaru P, Dimotakis P (1993) The lift of a cylinder executing rotary motions in a uniform flow. *J Fluid Mech* 255:1–10
- Unal M, Rockwell D (1988) On vortex formation from a cylinder. Part 2. Control by splitter-plate interference. *J Fluid Mech* 190:513–529
- Williamson C (1992) The natural and forced formation of spot-like 'vortex dislocations' in the transition of a wake. *J Fluid Mech* 243:393–441
- Williamson C (1996) Vortex dynamics in the cylinder wake. *Annu Rev Fluid Mech* 28:477–539
- Xu JC, Sen M, Gad-el Hak M (1990) Low-Reynolds number flow over a rotatable cylinder-splitter plate body. *Phys Fluids A Fluid Dyn* 2(11):1925–1927

Publisher's Note Springer Nature remains neutral with regard to jurisdictional claims in published maps and institutional affiliations.